Air-Stable, Nanostructured Electronic and Plasmonic Materials from Solution-Processable, Silver Nanocrystal Building Blocks

Aaron T. Fafarman,[†,○,#] Sung-Hoon Hong,[†,△,#] Soong Ju Oh,[§] Humeyra Caglayan,[†,¶] Xingchen Ye,[‡] Benjamin T. Diroll,[‡] Nader Engheta,[†,§,⊥,∥] Christopher B. Murray,[‡,§] and Cherie R. Kagan[†,‡,§,*]

[†]Department of Electrical and Systems Engineering, [‡]Department of Chemistry, [§]Department of Materials Science and Engineering, [⊥]Department of Physics and Astronomy, and [∥]Department of Bioengineering, University of Pennsylvania, Philadelphia, Pennsylvania 19104, United States. [#]A. T. Fafarman and S.-H. Hong contributed equally. [○]Present address: Dept. of Chemical Engineering, Drexel University, Philadelphia, Pennsylvania, United States. [△]Present address: Components & Materials Research Laboratory, Electronics and Telecommunication Research Institute (ETRI), Daejeon 305-350, Republic of Korea. [¶]Present address: Department of Electrical and Electronics Engineering, Abdullah Gul University, 38039 Kayseri, Turkey.

ABSTRACT Herein we describe a room-temperature, chemical process to transform silver nanocrystal solids, deposited from colloidal solutions, into highly conductive, corrosion-resistant, optical and electronic materials with nanometer-scale architectures. After assembling the nanocrystal solids, we treated them with a set of simple, compact, organic and inorganic reagents: ammonium thiocyanate, ammonium chloride, potassium hydrogen sulfide, and ethanedithiol. We find that each reagent induces unique changes in the structure and composition of the resulting solid, giving rise to films that vary from insulating to, in the case of thiocyanate, conducting with a remarkably low resistivity of $8.8 \times 10^{-6}\ \Omega \cdot$ cm, only 6 times that of bulk silver. We show that thiocyanate mediates the spontaneous sintering of nanocrystals into structures with a roughness of less than 1/10th of the wavelength of visible light. We demonstrate that these solution-processed, low-resistivity, optically smooth films can be patterned, using imprint lithography, into conductive electrodes and plasmonic mesostructures with programmable resonances. We observe that thiocyanate-treated solids exhibit significantly retarded atmospheric corrosion, a feature that dramatically increases the feasibility of employing silver for electrical and plasmonic applications.

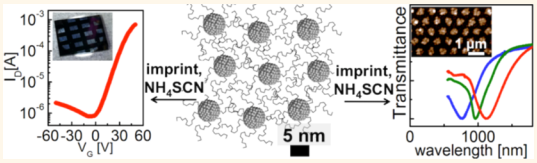

KEYWORDS: silver nanoparticles · ligand exchange · ammonium thiocyanate · conductivity · dielectric function · metamaterials · nanoimprinting · soft lithography · printing · electrodes

Silver is the most electrically conductive metal, rendering it an ideal choice for wires and electrodes in electronic applications, such as printed electronic circuitry,[1−3] photovoltaics,[4] and radio frequency identification tags,[5] and for plasmonic structures in optical applications, such as surface-enhanced Raman scattering (SERS)-based biosensors[6−8] and optical metamaterials.[9] For each of these applications there is a technological drive to find increasingly inexpensive means of fabricating the conductive components over large areas, on a wide range of substrates, and with high throughput. A common approach to this problem has been to print or cast a liquid containing silver particles or molecular precursors, often dubbed a "silver ink", into a desired structure and to use heat or chemical agents to sinter the ink and form a conductive solid.[2,3,10−15]

A common formulation of the inks begins with silver nanocrystals, synthesized in organic solvents in the presence of a hydrocarbon surfactant, an approach we adopt for this study.[1] Such synthetic methods provide exquisite control of the size and shape of the nanocrystals,[16] allowing for complex bottom-up self-assembly, as in the case of superlattice formation.[17−19] The nanocrystals are also stable in a range of solvents of different viscosities and boiling points ideal for several different wide-area, top-down fabrication modalities, including spin-coating, dip-coating, inkjet printing, and nanoimprinting.[10,20−22] However, after evaporation of the solvent, the nanocrystal solids are highly insulating, as electrons cannot easily be transported between particles across the long, insulating hydrocarbons. To address this limitation, researchers

* Address correspondence to kagan@seas.upenn.edu.

Received for review December 17, 2013 and accepted January 31, 2014.

Published online January 31, 2014
10.1021/nn406461p

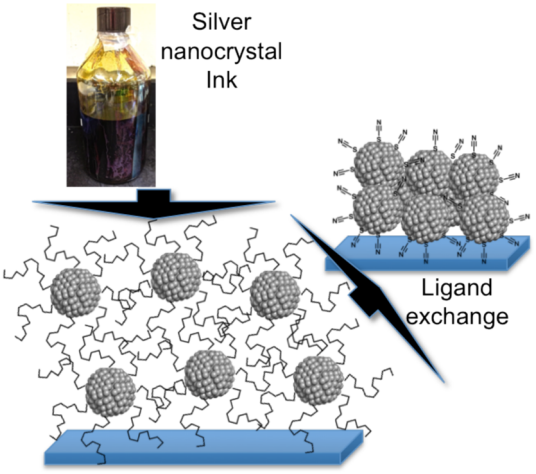

Scheme 1. Silver nanocrystal ink, deposited on a substrate, with subsequent chemical exchange of the hydrocarbon ligands for the compact thiocyanate.

have turned to methods to exchange the hydrocarbons for more compact surface ligands after deposition.[17]

In this study, we explore a set of four related, yet chemically distinct, compact ligands: ammonium thiocyanate (NH_4SCN), recently introduced by us as a ligand exchange agent[23] and depicted in Scheme 1; potassium hydrogen sulfide (KHS);[24] ammonium chloride (NH_4Cl), an alternative halide salt to those used previously;[12,15,25] and the well-studied ethanedithiol (EDT).[26,27] This set of ligand chemistries allows us to compare inorganic sulfides to an alkyl sulfide, monovalent to divalent sulfides, and monovalent sulfide to halide in their reactivity toward silver nanocrystals. We show that differences in the chemical interactions between the ligands and the silver drive dramatic variations in the structure and composition of the resulting solids and, consequently, in their electrical and optical properties as well. As has been observed previously with chloride salts,[12,15,25] NH_4SCN treatment initiates rapid, room-temperature sintering of the nanocrystals, yielding remarkably low resistivity silver solids. However, despite identical charge, valency, and counterion, thiocyanate uniquely mediates controlled grain growth, producing structures that are smooth on the length scale of visible light. We demonstrate the utility of low-resistivity, optically smooth thiocyanate-treated silver nanocrystal solids by employing imprint lithography to form the electrodes of high-performance nanocrystal field-effect transistors (FETs) and the plasmonic components of optical metamaterials.

Although prized for its low resistivity toward both direct current (dc) and optical displacement currents, bare silver suffers from sulfidation from atmospheric sulfur sources at a rate of 6 nm per month,[28] and nanostructured silver corrodes as much as 7 times faster.[29] We observe that the NH_4SCN-treated silver nanostructures are significantly more stable toward atmospheric corrosion than the examples of bare silver in the literature.[29,30] Thiocyanate-treated, silver nanocrystal thin films show only small changes in dc resistivity, and nanocrystal-based, optical metamaterials exhibit plasmonic resonances that are invariant over weeks of storage under atmospheric conditions, demonstrating new possibilities for nanostructured silver conductors wherever corrosion would otherwise preclude their use.

RESULTS AND DISCUSSION

Transmission Fourier transform infrared (FT-IR) spectra were used to follow the extent of ligand exchange upon treatment of the silver nanocrystal films with NH_4SCN, NH_4Cl, KHS, or EDT (Figure 1A). For each of the inorganic reagents, the peaks observed in the 2900 cm^{-1} region of the spectrum of the as-deposited film (black), due to CH-stretching transitions, were reduced by more than 95%; for the EDT-treated sample (red), they were reduced, consistent with the smaller number of methylene units in the new ligand. NH_4SCN (blue) treatment introduced a new peak in the IR spectrum at 2100 cm^{-1}, characteristic of the CN triple-bond stretch. The peak was significantly blue-shifted and broadened relative to that for solid NH_4SCN at 2050 cm^{-1} and was not accompanied by the NH stretches observed for the ammonium group around 3300 cm^{-1}, suggesting that the anionic thiocyanate was chemisorbed to positive charge sites on the nanocrystal surface.[23] This same binding mode was previously reported for thiocyanate adsorbed on polished polycrystalline silver surfaces.[31]

It has been observed that immersing silver nanoparticles in electrolyte solutions, particularly chlorides, can stimulate particle sintering and grain growth, even at room temperature.[12,25] We monitored the changes chemically induced at room temperature in the composition and grain structure of our nanocrystal films by wide-angle X-ray scattering and atomic force microscopy (AFM). The X-ray patterns (Figure 1B) for the as-deposited nanocrystal solids (black), as well as those treated with EDT (red), exhibited broad reflections characteristic of isolated 5 nm diameter crystals. In contrast, NH_4Cl (green) and NH_4SCN (blue) treated silver nanocrystals showed dramatic narrowing of the scattering peaks, indicative of significant grain growth. KHS (magenta) treatment resulted in an entirely different scattering pattern, characteristic of the acanthite phase of silver sulfide.[32] A similar conversion reaction from silver to acanthite was reported for silver nanoparticles exposed to hydrogen sulfide gas.[33] For the NH_4Cl- and NH_4SCN-treated samples, evidence of nanocrystal coalescence was readily observed by AFM, consistent with the crystallite grain growth observed in X-ray diffraction studies. Before treatment, the nanocrystal films showed a smooth surface, with roughness

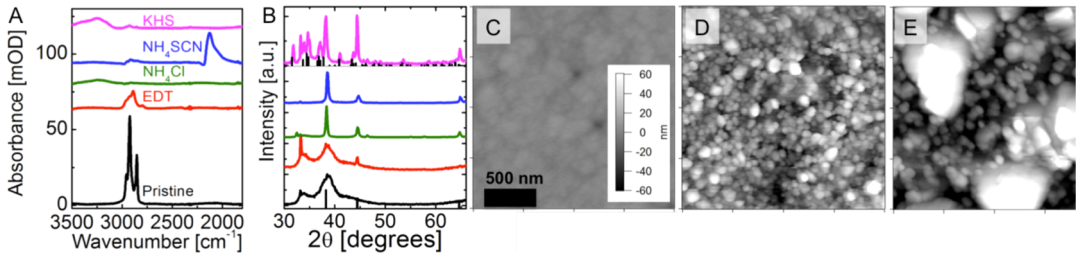

Figure 1. Chemical and structural properties of silver nanocrystal thin films, before and after ligand exchange. (A) FT-IR absorption spectra and (B) wide-angle X-ray scattering patterns for silver nanocrystal films before ligand exchange (black) and after exchange with EDT (red), NH_4Cl (green), NH_4SCN (blue), and KHS (magenta). Also shown in (B) are database values for the scattering peaks of silver and acanthite (Ag_2S) in black bars. AFM images of silver nanocrystal films, (C) before exchange and after exchange with (D) NH_4SCN and (E) NH_4Cl. The *z*-height scale bar in the inset of panel C applies to panels C–E. The deposition conditions in each case were as follows: spin-coating at 30 mg/mL (A), dropcasting at 100 mg/mL (B), spin-coating at 75 mg/mL (C–E).

TABLE 1. Resistivity of Silver Nanocrystal Thin Films Determined by Four-Point Probe Method

	evaporated silver	EDT treated	KHS treated	NH_4Cl treated	NH_4Cl treated (3 layers)	NH_4SCN treated	NH_4SCN treated (3 layers)
resistivity [$\times 10^{-6}$ Ω·cm]	1.9 ± 0.4	(6 ± 2) × 10^5	insulating[a]	insulating[a]	12 ± 5	150 ± 60	8.8 ± 2
thickness[b] [nm]	70 ± 5	~130	not determined[c]	150 ± 7	370 ± 90	180 ± 6	220 ± 20

[a] Resistance of the film measured between electrode pairs was out of the range of the instrument, *e.g.*, greater than 1 MΩ. [b] Thickness is reported as the average of three independently prepared samples, and in the case of NH_4Cl, the sampled regions were chosen to exclude isolated, micrometer-scale particles. [c] Upon exposure to KHS, the films start to buckle and wrinkle, making it difficult to find a pristine span of material to perform the AFM thickness measurement.

on the order of the 5 nm average diameter of the original nanocrystals (Figure 1C). NH_4SCN treatment caused the individual nanocrystals to coalesce into larger, approximately 60 nm diameter grains, with a relatively narrow distribution in size, as seen in Figure 1D. In contrast, NH_4Cl-treated nanocrystals evolved into grains with a bimodal distribution in size. The majority of the silver was found in micrometer-sized particles interspersed among nanoscale particles, resulting in discontinuous islands of silver on the surface, as seen in a representative AFM image in Figure 1E. The bimodal distribution is consistent with Ostwald ripening occurring in the presence of chloride. All of these changes in grain size and structure occur at room temperature, without any annealing steps. In the case of NH_4SCN, we hypothesize that the 10^2-fold higher affinity of thiocyanate for silver, compared to that of chloride,[34] may offer a countervailing driving force that balances the gradient in surface energy, which would otherwise drive runaway grain growth.

The observed compositional and structural variations upon chemical transformation resulted in dramatic and easily understood differences in the electrical resistivity of the treated films. Table 1 shows the resistivities of treated films measured by the four-point probe method, converted into bulk resistivities using the film thickness measured by AFM. Applying this technique to films of thermally evaporated silver, we observed resistivity within a factor of 1.2 of the literature value for bulk silver. Untreated silver nanocrystal films exhibited resistivity higher than the sensitivity of our four-point probe measurement tool (>MΩ·cm). EDT treatment brought the resistivity of the film within a measurable range, but the resistivity was still a factor of 10^5 higher than that of bulk silver, as expected given the approximately 1 nm interparticle spacing enforced by the two methylene units of the ligand.[26] KHS treatment resulted in an insulating film, consistent with the semiconducting nature of Ag_2S. A single coating of silver nanocrystals treated with NH_4Cl also exhibited insulating behavior, which is readily explained by the film structure, typified by discontinuous particles on the surface (Figure 1E). The voids in the structure can be filled by performing three successive spin-coating and exchange cycles, upon which the films showed very low resistivity: only 7.5 times higher than that of bulk silver. In contrast, even a single cycle of spin-coating and treatment with NH_4SCN provided conductive films owing to the dense and uniform grain growth, which yielded regular particles packed into a continuous solid (Figure 1D). Thicker films, made by spincasting and treating three successive layers, made the film yet more dense, yielding the lowest resistivity measured: only 5.5 times that of bulk silver. AFM images of single- and triple-layer nanocrystal films, deposited from colloidal silver nanocrystal dispersions of varying concentration and treated with NH_4SCN or NH_4Cl, are shown in Supporting Information Figure S1. In all cases we see that the NH_4SCN-treated films do not grow linearly in thickness with the number of layers deposited; instead the films grow in density as the variegated surface is increasingly infilled by subsequent layers (Table 1 and Supporting Information Figure S1).

The simple, chemical process outlined above, using inexpensive, relatively benign reagents, could be tuned to yield a remarkably conductive metallic solid from a

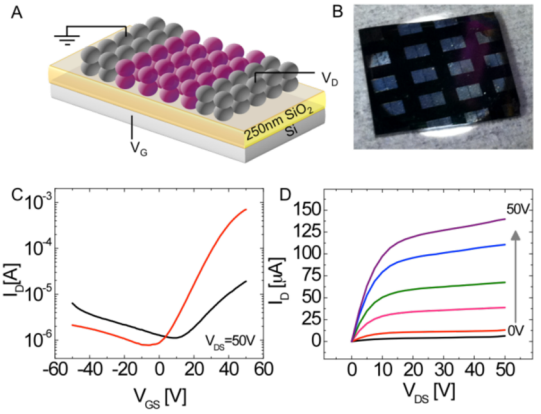

Figure 2. (A) Schematic of a field-effect transistor (FET) and (B) photograph of an array of FETs composed of PbSe nanocrystal semiconductor channels and solution-printed silver nanocrystal source and drain electrodes. (C) Transfer characteristics of an FET with V_D = 50 before (black) and after (red) 3 Å of Pb deposition. (D) Output characteristics of the Pb-rich FET.

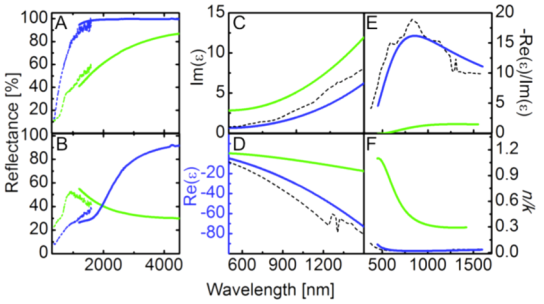

Figure 3. Optical properties of spin-coated silver nanocrystal films. Reflectance of silver nanocrystal thin films treated with (A) NH_4SCN or (B) NH_4Cl. Silver nanocrystals were spin-cast (100 mg/mL) and then exchanged, either one time to form a single layer (green) or three times sequentially to form three layers (blue). Dashed curves were measured on an ellipsometer, and solid curves were measured on an FT-IR spectrometer. (C,D) Real and imaginary permittivity of NH_4SCN-treated silver nanocrystal films, extracted from modeling the complex ellipsometric reflectivity as described in the Methods. Single- or triple-layer films are shown in green and blue, respectively. Reference data for bulk silver from Palik[38] (dashed, black curve). (E, F) Figures of merit for plasmonic materials derived from the permittivity shown in panels C and D, using the same coloring.

liquid precursor, opening broad avenues for technological exploitation. As the first demonstration we chose an important application in the field of electronics fabrication: imprint lithography to create conductive metal structures. In Figure 2 we show (A) a schematic and (B) a photograph of an array of PbSe nanocrystal FETs with bottom source and drain electrodes fabricated by spin-coating silver nanocrystals atop a resist patterned by imprint lithography, with subsequent NH_4SCN treatment and lift-off steps. PbSe nanocrystals of 6 nm diameter were then deposited by spin-coating and also treated with NH_4SCN to form the semiconducting channels. In this demonstration, the drain current was modulated with both positive and negative gate voltages (Figure 2C, black; typical output characteristics shown in Supporting Information Figure S2). The device exhibited a saturation electron mobility of 0.08 $cm^2/(V\ s)$ and hole mobility of 0.015 $cm^2/(V\ s)$, typical of ambipolar PbSe nanocrystal FETs without intentional doping.[35] To enhance the device performance, we employed our previously reported method of controlling the stoichiometry of the nanocrystal FETs by depositing 3 Å of Pb on the film, to make an n-type unipolar device.[36] The electron mobility was enhanced (Figure 2C, red) up to 5.1 $cm^2/(V\ s)$, comparable to the best PbSe nanocrystal FETs in the recent literature.[36,37] Output characteristics, shown in Figure 2D, rise linearly at low voltage, characteristic of low resistance at the silver/PbSe contacts, a significant achievement for printed electronics due to the sensitivity of FET performance to the quality of the electrical contact made at the metal−semiconductor interface.

Plasmonics and other optical applications require not only high conductivity of displacement currents but also structures that are smooth and uniform on a size scale smaller than the wavelength of light. In this respect, the control over grain size and uniformity afforded with NH_4SCN-treated silver nanocrystals represents a breakthrough over other chemically and thermally sintered inks. Figure 3 shows a comparison of the reflectivity of (A) NH_4SCN- *versus* (B) NH_4Cl-treated silver nanocrystal films that illustrates the advantages of limited grain size. For thiocyanate, a single cycle of spin-coating and exchange (green) afforded a film that exhibited an asymptotic rise in reflectivity toward 100% with increasing wavelength, as expected for a Drude oscillator. In contrast, the chloride case shows a small peak in reflectivity around 1000 nm that we assign to resonant scattering off the micrometer-scale structures and declining reflectivity toward the far-IR, consistent with dc electrical measurements that showed it to be insulating (Table 1). In both cases, performing three cycles of spincasting and exchange (blue) densified the films by partially filling the voids. This afforded films with reflectivity approaching 100% in the mid-IR, consistent with their very high dc conductivity (Table 1). However, in the case of chloride, in the visible to near-IR, the wavelength of light is comparable to the size of the micrometer-scale silver grains and strong, diffuse scattering would be expected; accordingly we observed very poor specular reflectivity in this range compared to the smoother thiocyanate-treated films.

For use as a plasmonic building block for metamaterials, EDT- and KHS-treated nanocrystal films were insufficiently conductive, while NH_4Cl treatment caused uncontrolled grain growth, making it unfeasible to fabricate nanoscale features. The combination of high conductivity and structural control afforded by NH_4SCN treatment was unique among the set of ligands tested, prompting us to further evaluate the merits of NH_4SCN-treated silver solids for optical applications by

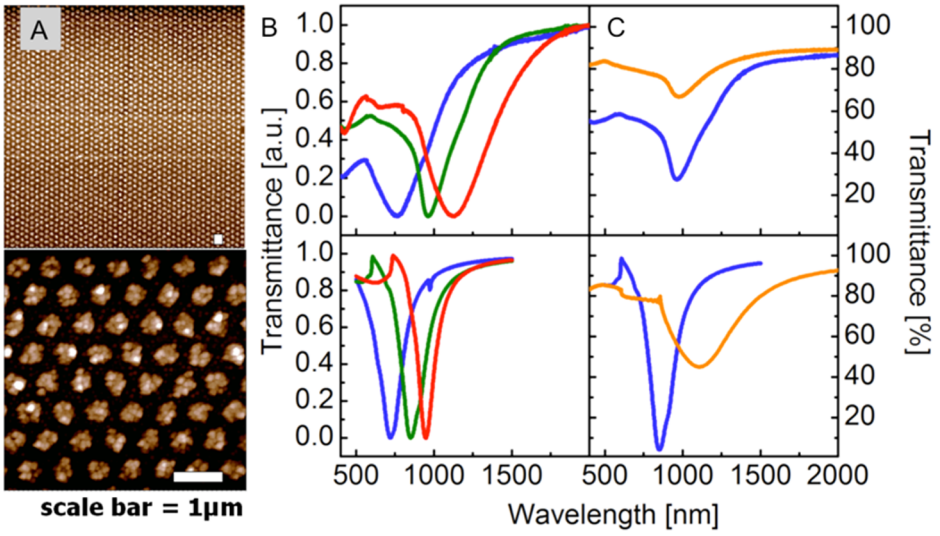

Figure 4. Nanoimprinted nanocrystal-derived nanodisk arrays treated with ammonium thiocyanate. (A) AFM images of nanoimprinted silver nanocrystal nanodisk arrays. (B) Top: Transmittance spectra of arrays of different diameter and spacing. Bottom: FDTD simulation of the transmittance. Blue, green, and red correspond to disks printed from templates with diameters and spacings of 200/500, 270/700, and 300/850 nm, respectively. Curves have been normalized. (C) Top: Measured transmittance spectra of silver and gold nanocrystal-derived superstructure arrays, in blue and orange, respectively, with a diameter/spacing of 270/700 nm. Bottom: Simulated transmittance using values from ellipsometry. Gold data taken from ref 21.

determining their complex electrical permittivity. We obtained the real and imaginary permittivity of the NH_4SCN-treated silver nanocrystal films through modeling of spectroscopic ellipsometry data, shown in Figure 3C and D, respectively (see the Methods section for details and Supporting Information Figure S3 for the raw and modeled complex reflectivity data). The green and blue curves are representative permittivity functions for one and three successive spin-coated and NH_4SCN-treated layers of nanocrystals, respectively. The dashed black line provides a reference for bulk silver films and is reproduced from Palik.[38] In comparison to the three-layer spin-coated sample, which shows real and imaginary permittivity akin to that of bulk silver, the single spin-coated layer exhibited less negative values of the real part of the permittivity, as expected based on the higher dc resistivity (Table 1) and lower IR reflectivity (Figure 3A). The single layer showed larger values of the imaginary part of the permittivity, consistent with greater dissipative losses due to the rougher surface (Supporting Information Figure S1).

We used two different common figures of merit to evaluate the fitness of these materials for plasmonic and metamaterial applications. The negative of the ratio of the real and imaginary components of the permittivity $[-\mathrm{Re}(\varepsilon)/\mathrm{Im}(\varepsilon)]$ is a figure of merit for localized surface plasmon applications, and it quantifies the strength of the coupling of the electric field, relative to the losses due to absorption in the material.[39,40] A conceptually similar but quantitatively distinct figure of merit has been proposed for hyperbolic metamaterials: the ratio of the real and imaginary components of the index of refraction $[n/k]$.[40] We used both measures to compare the quality of NH_4SCN-treated silver nanocrystal films, typified by single (green, Figure 3C,D) and triple (blue, Figure 3C,D) spin-coated films to bulk silver (black, Figure 3C,D). $-\mathrm{Re}(\varepsilon)/\mathrm{Im}(\varepsilon)$ and n/k are shown in Figure 3E and F, respectively. By these measures the triple-layer, solution-processed nanocrystal films were roughly equal in quality to bulk silver. Single-layer films couple less strongly to the light field due to their less negative, real permittivity, in addition to having higher dissipative losses.

Combining the advantages of bulk-like optical and electrical properties with the practical facility of using solution-processed building blocks, we tackled the problem of wide-area, room-temperature fabrication of subwavelength plasmonic structures by nanoimprint lithography. As in the case of the FET electrodes above, hexagonal arrays of disks of silver superstructures, 200−300 nm in diameter, were fabricated by spin-coating silver nanocrystals atop a resist, patterned by imprint lithography, with subsequent NH_4SCN treatment and lift-off. In Figure 4A, the nanocrystal-derived nanodisk superstructures can be seen to be composed of small, <100 nm diameter silver grains, similar to those observed in spin-cast, NH_4SCN-treated thin films (Figure 1D). The optical transmittance spectra of the disk arrays are shown in Figure 4B,C. Varying the diameter and pitch of the arrays leads to one dominant, broadly tunable resonance that ranges from the edge of the visible, well into the near-IR (Figure 4B, top panel). Inspection of the individual nanodisk superstructures in the array in Figure 4A revealed unintentional roughness due to coalescence of the nanocrystals into larger silver grains. We performed finite-difference, time domain (FDTD) simulations to compare the theoretical to the

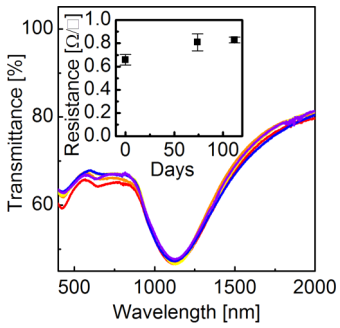

Figure 5. Electrical and optical properties of NH_4SCN-treated silver nanocrystal solids stored in ambient laboratory conditions. Transmittance of a nanoimprinted, nanocrystal-derived, nanodisk superstructure array such as that shown in Figure 4 over 20 days. Films were measured immediately after fabrication (red) and after 2 h and 1, 2, 10, and 20 days in orange, yellow, green, blue, and purple, respectively. (Inset) Sheet resistance for a sample composed of three spin-cast layers.

observed transmittance, using only the experimentally measured dielectric functions for the silver nanocrystal-derived thin films and the geometric parameters of the array. The simulations accounted for roughness by defining each disk in the unit cell with a randomly roughened surface (see the Methods section for details and Supporting Information Figure S4 for a comparison showing the effect of adding roughness). The simulated transmittance spectra qualitatively capture the different resonant wavelengths of the plasmonic features and the trend with increasing diameter (Figure 4B, bottom panel).

As a choice of potential building blocks for nanoimprinted plasmonic structures, it is interesting to compare the present result with those we obtained previously on NH_4SCN-treated gold nanocrystal superstructure arrays.[21] In the top panel of Figure 4C, it was seen that for superstructure arrays of the same diameter and pitch composed of either silver (blue) or gold (red) nanocrystals, each treated with NH_4SCN, the plasmonic resonance feature around 1000 nm was much different in amplitude. The larger cross-section for the sample constructed from silver nanocrystals was readily apparent in FDTD simulations as well. This is a consequence of the more negative, real part and smaller imaginary part of its measured dielectric constant, which dictate a stronger coupling to the optical field and narrower resonance, respectively. NH_4SCN-treated gold nanocrystals were observed previously to "neck",[21] rather than to completely coalesce as silver nanocrystals do, resulting in a larger void volume for gold. It is worth pointing out that the ratio of the resistivity of bulk gold to bulk silver is only 1.5, whereas the structural differences between NH_4SCN-treated gold and silver nanocrystal films lead to a ratio of their respective resistivities >5. For purposes of designing metamaterials, the gold nanocrystals can be regarded as building blocks for a "dilute metal" for applications where the permittivity must be negative, but not too negative; the silver nanocrystal solids more closely resemble bulk metals.

We studied the air-stability of the electrical and optical properties of NH_4SCN-treated silver nanocrystal-based materials and found significant retardation of atmospheric corrosion. The dc sheet resistance of films such as those in Table 1, stored in laboratory air, remained within 20% of its minimum value for the entire interval test of over 100 days (Figure 5, inset). More dramatically, the plasmonic features remained stable over the interval tested of 20 days, as shown in Figure 5. Although direct comparison between dc resistivity and high-frequency optical resonance is not possible, as they are influenced by different scattering mechanisms, in Supporting Information Figure S5, we compare both metrics of atmospheric stability by plotting the relative changes in resistivity and the width and energy of the optical resonance on the same time scale. Focusing on the optical data, we emphasize that they are in stark contrast with literature reports of the plasmonic resonances of bare silver nanodisks red-shifting at a rate of 43 nm per day as a result of atmospheric corrosion.[29] We note that samples such as the one shown in Figure 5 accumulate multiple hours of on- or nearly on-resonance irradiation in the course of the UV–vis transmission experiment, during which time they receive an average flux of approximately 10 $\mu W/cm^2$, without observable spectral changes. This indicates that ohmic heating due to optical displacement currents at these fluxes is not sufficient to damage the structures. Additionally no special care is taken to protect the samples from room light. However, we observe that the plasmonic resonances begin to change significantly above 80 °C. The origin and limits of the stability of our nanostructures are the subjects of ongoing study. A similar effect whereby silver nanoparticles were stabilized against oxidative dissolution by the presence of halide ions in solution was previously observed and attributed to the insoluble, stable silver halide salt being deposited on the nanoparticle surface, thus passivating the core.[41,42] We speculate that a similar process occurs here with the "pseudo-halide" thiocyanate. It is also worth noting that thiocyanate is a component in many metal polishes and corrosion inhibitors.[43,44] Regardless of the mechanism, circumventing the problem of rapid corrosion of nanostructured silver will be of great technological value.

CONCLUSIONS

Chemical interactions between small molecules and colloidal silver nanocrystals are exquisitely specific and dramatically influence the compositional, structural, electrical, and optical properties of silver nanocrystal solids. Thiocyanate, with its strong affinity for silver, mediates regular, size-focused crystal growth from the original nanocrystal building blocks, forming highly conductive structures. Sulfide on the other hand has an even greater affinity for silver, in addition to different

valency, and both differences may influence its tendency to instead transform silver nanocrystals into Ag_2S. As a novel material, thiocyanate-treated silver nanocrystal solids possess optical and electrical features for electrical and plasmonic applications of comparable utility to evaporated silver, with the added advantage of enhanced stability against corrosion. The facility with which this material can be deposited on an arbitrary substrate, under ambient temperature and atmospheric conditions, using only noncaustic, inexpensive, and relatively environmentally benign starting materials suggests great promise for technological applications.

METHODS

Synthesis. Silver nanocrystals of 5 nm were synthesized using a microwave reactor (CEM Discover) running in open-vessel mode as described previously.[19] Typically, 1 mmol of tetradecylphosphonic acid (PCI synthesis), 2 mmol of silver acetate (Aldrich), and 20 mL of trioctylamine (Aldrich) were loaded into a 50 mL round-bottomed flask. Under a nitrogen atmosphere and vigorous stirring, the reaction mixture was heated by microwave irradiation (150 W) to 150 °C in 4 min and held at 150 °C for another 5 min. The reaction flask was air-cooled to room temperature. After synthesis all subsequent steps were carried out in ambient air conditions. To purify the product, the nanocrystals were first flocculated by adding ethanol and isolated by centrifugation. Nanocrystals were subsequently dispersed in hexane, flocculated a second time using isopropyl alcohol, and isolated by centrifugation to ensure the complete removal of excess tetradecylphosphonic acid and trioctylamine. The nanocrystals were dispersed in octane for spin-casting.

Deposition and Ligand Exchange. Glass and silicon substrates were cleaned and coated with a self-assembled monolayer of 3-mercaptopropyl-trimethoxysilane (MPTS) to aid the adhesion of the nanocrystals after exchange, according to our previously published protocol and references therein.[21] Uniform, unpatterned nanocrystal thin films for FT-IR and variable-angle ellipsometric spectroscopies, AFM, and dc conductivity measurements were prepared by spin-casting. Then 30, 75, or 100 mg/mL dispersions of nanocrystals in octane were filtered through a 0.2 μm polytetrafluoroethylene filter and spin-cast at 500 rpm for 60 s onto MPTS-coated substrates. The substrates appropriate for each measurement were as follows: double-sided polished silicon for FT-IR transmittance, single-sided polished silicon with 250 nm thermal oxide for conductivity, AFM, ellipsometry, and FT-IR reflectance, and glass for vis−NIR transmittance. Samples for wide-angle X-ray scattering experiments were prepared by drop-casting micrometer-thick nanocrystal films on single-sided polished silicon with a native oxide.

Ligand exchange was performed after spin-casting or nanoimprinting by immersing the nanocrystal-coated substrate in a methanol solution containing the new ligand. Nonspecifically bound ligand was washed off the surface by immersing the sample in two successive baths of pure methanol and drying it in air. For triple-layer films, one cycle of deposition, exchange, and washing was repeated three times, sequentially. Ethanedithiol was prepared as a 1% (v/v) solution in methanol, and exchange was carried out for 3 h. For NH_4SCN and NH_4Cl the conditions were either 50 mM for 10 min or 130 mM for 2 min. An equivalent extent of exchange was observed for both cases. For potassium hydrogen sulfide the conditions were 50 mM for 10 min. Substantial delamination of large flakes of material off of the substrate occurs with sulfide treatment. *Note: potassium hydrogen sulfide can produce noxious hydrogen sulfide gas; use this reagent only with adequate ventilation and do not allow the waste to become acidified.*

Imprint Lithography. NXR-1000 thermal imprint resist (Nanonex) was spin-coated at 3000 rpm for 1 min onto glass substrates prepared as described above and prebaked at 150 °C for 5 min. A master template consisting of either an array of nanodisks or an array of pairs of electrodes was placed on the substrate. The master template, thermal resist, and substrate stack was heated to 130 °C and compressed at 300 psi for 5 min, cooled to room temperature, and demolded in the Nanonex NX-2600 nanoimprint tool. An oxygen plasma-based descumming process was performed on the patterned substrate to remove any thin, residual layer in the bottom of the imprinted wells. The silver nanocrystal dispersion was spin-coated on the imprinted patterned substrate. Ligand exchange was carried out by dipping the substrate into 130 mM ammonium thiocyanate in methanol. Washing was performed by transferring the sample directly to a bath of clean 2-propanol. Finally, the imprinted resist was removed by lift-off in acetone with sonication for 1 min, leaving the nanopatterned silver nanocrystal-derived superstructure array of disks or electrodes on the glass substrate.

FET Fabrication. FET devices were fabricated on heavily n-doped silicon wafers with 250 nm thermally grown SiO_2. Silver nanocrystal source and drain electrodes were deposited by imprint lithography as described above. PbSe nanocrystals (6 nm) were synthesized using a slight modification of a previously reported procedure.[45] A solution of 10 mg/mL PbSe nanocrystals in octane was spin-coated at 1000 rpm to deposit a uniform nanocrystal thin film solid, and the substrates were immersed in 130 mM NH_4SCN in methanol for 30s and then immersed in two successive baths of pure methanol. The spin-coating and ligand treatment were repeated twice to achieve a thickness of ~30 nm. To make n-type, Pb-rich PbSe nanocrystal thin films, 3 Å of Pb was deposited with the rate of 0.01−0.03 Å/s using a thermal evaporator integrated into a nitrogen glovebox.

Characterization. FT-IR was performed on a Nicolet 6700 (Thermo Scientific) spectrometer with a mercury cadmium telluride detector, for transmittance, or a deuterated triglycine sulfate detector for reflectance. AFM was performed in ac mode with an MFP-3D-BIO microscope (Asylum Research Corp.) using an AC240TS silicon cantilever (Olympus). Film thickness was measured as the average of three identically prepared samples. For chloride-treated samples, areas with large, isolated, micrometer-scale grains were excluded from the thickness calculation. Roughness was estimated from the root-mean-square deviations around the average thickness. Wide-angle X-ray scattering measurements were performed on a Rigaku Geigerflex diffractometer, using copper K-alpha X-rays, operated at 40 kV and 35 mA. The dc conductivity was measured using a linear four-point probe with 1 mm voltage−probe spacing and 3 mm current−probe spacing (Cascade Microtech). Sheet resistivities were translated into bulk resistivities using AFM-measured film heights. FET characterization was carried out on a model 4156C semiconductor parameter analyzer (Agilent) in combination with a Karl Suss PM5 probe station mounted in a nitrogen glovebox. The transmittance spectra of the lithographically patterned arrays were measured with a Cary 5000 UV−vis−NIR spectrophotometer (formerly Varian Inc., now Agilent Technologies) without polarization, with 2 nm spectral bandpass, and are reported after subtraction of a background consisting of a blank substrate. Variable-angle ellipsometry spectra of uniform nanocrystal films on polished silicon substrates were measured using an M-2000 ellipsometer (J.A. Woollam Co.). The complex reflectance ratio was measured from 370 to 1680 nm at angles of 55°, 65°, and 75°. To extract the dielectric functions, these complex reflectance spectra were modeled using the CompleteEASE software package (J.A. Woollam Co.). To address the surface roughness, the software's default "roughness model" was invoked, which includes two distinct layers: one uniform underlayer to describe the treated silver nanocrystal material and, above it, a "rough" layer, modeled as air intermixed with the material of the underlayer, using an effective medium approximation. The optical properties of the underlayer were modeled using a combination of a Drude oscillator, to describe the

oscillations of the free electrons, and a sum of three harmonic oscillators, to describe the transitions of the bound electrons. The resistivity and scattering time of the Drude oscillator were fit as free parameters and refined to values within 20% of the dc-measured resistivity in the case of the triple-layer films. In the case of the single layer, the Drude resistivity was fixed to the value from the dc measurement to further constrain the fit. The parameters to define the bound electron transitions were taken from the database of values provided in CompleteEASE for bulk silver. Either the roughness was also fit as a free parameter and refined to within a factor of 2 of the AFM measured roughness, or the measured roughness was used as a fixed parameter of the model. The ellipsometrically derived dielectric function used in the simulations is that of the uniform underlayer, with the surface roughness taken out. The complex reflectance spectra and additional modeling details can be found in Supporting Information Figure S3. To construct a wide-range spectrum of the reflectance intensity, the data in the vis−NIR range from the ellipsometer were stitched together with data acquired in the near-to-mid-IR using a Seagull Variable Angle Reflection Accessory (Harrick Scientific Products) on the Nicolet 6700 FT-IR spectrometer.

Simulation. Full-field electromagnetic wave calculations were performed using a commercially available FDTD simulation software package from Lumerical Solutions, Inc. A unit cell of the investigated structure was simulated using periodic boundary conditions along the *x* and *y* axes and perfectly matched layers along the propagation of electromagnetic waves (*z* axis). Plane waves were launched incident to the unit cell along the $+z$ direction, and transmittance was monitored with a power monitor placed behind the structure. Electric and magnetic fields were detected within the frequency profile monitors. All of the simulations reported in this paper were performed in three-dimensional layouts. To model the nanocrystal films in the simulations, we used the measured dispersion data for a triple-layer, thiocyanate-treated silver nanocrystal film. An array of perfectly cylindrical nanodisks was defined, and roughness was added to the surfaces. The roughness was defined as a specific correlation length of 15 nm in the *x*, *y*, and *z* directions; therefore each nanodisk in the unit cell has a unique, random rough surface.

Conflict of Interest: The authors declare no competing financial interest.

Acknowledgment. The authors thank Elizabeth Ashley Gaulding for synthesizing the PbSe nanocrystals used in this work. The synthesis of silver nanocrystals, nanoimprinting of silver nanocrystal-based superstructures and their ligand exchange, optical spectroscopy of nanocrystal-based nanostructures, ellipsometry, and FDTD simulations were supported by the Office of Naval Research Multidisciplinary University Research Initiative Award No. ONR-N00014-10-1-0942. The work on silver nanocrystal thin film deposition and ligand exchange, conductivity, atomic force microscopy, and PbSe nanocrystal FET fabrication and characterization was supported by the U.S. Department of Energy Office of Basic Energy Sciences, Division of Materials Science and Engineering, under Award No. DE-SC0002158. X-ray studies were supported by the NSF Solar Program under Award No. DMS-0935165. Scanning electron microscopy was performed in facilities supported by the NSF MRSEC Program under Award Number DMR-1120901.

Supporting Information Available: Additional AFM images and FET data, raw and modeled spectroscopic ellipsometry data, and additional FDTD simulation results. This material is available free of charge *via* the Internet at http://pubs.acs.org.

REFERENCES AND NOTES

1. Li, Y.; Wu, Y.; Ong, B. S. Facile Synthesis of Silver Nanoparticles Useful for Fabrication of High-Conductivity Elements for Printed Electronics. *J. Am. Chem. Soc.* **2005**, *127*, 3266–3267.
2. Walker, S. B.; Lewis, J. A. Reactive Silver Inks for Patterning High-Conductivity Features at Mild Temperatures. *J. Am. Chem. Soc.* **2012**, *134*, 1419–1421.
3. Polavarapu, L.; Manga, K. K.; Cao, H. D.; Loh, K. P.; Xu, Q.-H. Preparation of Conductive Silver Films at Mild Temperatures for Printable Organic Electronics. *Chem. Mater.* **2011**, *23*, 3273–3276.
4. Tvingstedt, K.; Inganäs, O. Electrode Grids for ITO Free Organic Photovoltaic Devices. *Adv. Mater.* **2007**, *19*, 2893–2897.
5. Nie, X.; Wang, H.; Zou, J. Inkjet Printing of Silver Citrate Conductive Ink on PET Substrate. *Appl. Surf. Sci.* **2012**, *261*, 554–560.
6. Shafer-Peltier, K. E.; Haynes, C. L.; Glucksberg, M. R.; Van Duyne, R. P. Toward a Glucose Biosensor Based on Surface-Enhanced Raman Scattering. *J. Am. Chem. Soc.* **2003**, *125*, 588–593.
7. Willets, K. A.; Van Duyne, R. P. Localized Surface Plasmon Resonance Spectroscopy and Sensing. In *Annual Review of Physical Chemistry*; Annual Reviews: Palo Alto, 2007; Vol. 58, pp 267−297.
8. Kodiyath, R.; Malak, S. T.; Combs, Z. A.; Koenig, T.; Mahmoud, M. A.; El-Sayed, M. A.; Tsukruk, V. V. Assemblies of Silver Nanocubes for Highly Sensitive SERS Chemical Vapor Detection. *J. Mater. Chem. A* **2013**, *1*, 2777–2788.
9. Dolling, G.; Enkrich, C.; Wegener, M.; Soukoulis, C. M.; Linden, S. Low-Loss Negative-Index Metamaterial at Telecommunication Wavelengths. *Opt. Lett.* **2006**, *31*, 1800–1802.
10. Lee, H.-H.; Chou, K.-S.; Huang, K.-C. Inkjet Printing of Nanosized Silver Colloids. *Nanotechnology* **2005**, *16*, 2436.
11. Perelaer, J.; Smith, P. J.; Mager, D.; Soltman, D.; Volkman, S. K.; Subramanian, V.; Korvink, J. G.; Schubert, U. S. Printed Electronics: The Challenges Involved in Printing Devices, Interconnects, and Contacts Based on Inorganic Materials. *J. Mater. Chem.* **2010**, *20*, 8446–8453.
12. Long, Y.; Wu, J.; Wang, H.; Zhang, X.; Zhao, N.; Xu, J. Rapid Sintering of Silver Nanoparticles in an Electrolyte Solution at Room Temperature and Its Application to Fabricate Conductive Silver Films Using Polydopamine as Adhesive Layers. *J. Mater. Chem.* **2011**, *21*, 4875–4881.
13. Magdassi, S.; Grouchko, M.; Berezin, O.; Kamyshny, A. Triggering the Sintering of Silver Nanoparticles at Room Temperature. *ACS Nano* **2010**, *4*, 1943–1948.
14. Wakuda, D.; Hatamura, M.; Suganuma, K. Novel Method for Room Temperature Sintering of Ag Nanoparticle Paste in Air. *Chem. Phys. Lett.* **2007**, *441*, 305–308.
15. Zapka, W.; Voit, W.; Loderer, C.; Lang, P. Low Temperature Chemical Post-Treatment of Inkjet Printed Nano-Particle Silver Inks. *NIP Digit. Fabr. Conf.* **2008**, *2008*, 906–911.
16. Park, J.; Kwon, S. G.; Jun, S. W.; Kim, B. H.; Hyeon, T. Large-Scale Synthesis of Ultra-Small-Sized Silver Nanoparticles. *ChemPhysChem* **2012**, *13*, 2540–2543.
17. Andres, R. P.; Bielefeld, J. D.; Henderson, J. I.; Janes, D. B.; Kolagunta, V. R.; Kubiak, C. P.; Mahoney, W. J.; Osifchin, R. G. Self-Assembly of a Two-Dimensional Superlattice of Molecularly Linked Metal Clusters. *Science* **1996**, *273*, 1690–1693.
18. Murray, C. B.; Sun, S.; Gaschler, W.; Doyle, H.; Betley, T. A.; Kagan, C. R. Colloidal Synthesis of Nanocrystals and Nanocrystal Superlattices. *IBM J. Res. Dev.* **2001**, *45*, 47–56.
19. Ye, X.; Chen, J.; Diroll, B. T.; Murray, C. B. Tunable Plasmonic Coupling in Self-Assembled Binary Nanocrystal Superlattices Studied by Correlated Optical Microspectrophotometry and Electron Microscopy. *Nano Lett.* **2013**, *13*, 1291–1297.
20. Choi, J.-H.; Lee, S.-W.; Jeong, J.-H.; Choi, D.-G.; Lee, E.-S. Direct Imprint of Conductive Silver Patterns Using Nanosilver Particles and UV Curable Resin. *Microelectron. Eng.* **2009**, *86*, 622–627.
21. Fafarman, A. T.; Hong, S.-H.; Caglayan, H.; Ye, X.; Diroll, B. T.; Paik, T.; Engheta, N.; Murray, C. B.; Kagan, C. R. Chemically Tailored Dielectric-to-Metal Transition for the Design of Metamaterials from Nanoimprinted Colloidal Nanocrystals. *Nano Lett.* **2013**, *13*, 350–357.
22. Rycenga, M.; Cobley, C. M.; Zeng, J.; Li, W.; Moran, C. H.; Zhang, Q.; Qin, D.; Xia, Y. Controlling the Synthesis and Assembly of Silver Nanostructures for Plasmonic Applications. *Chem. Rev.* **2011**, *111*, 3669–3712.

23. Fafarman, A. T.; *et al*. Thiocyanate-Capped Nanocrystal Colloids: Vibrational Reporter of Surface Chemistry and Solution-Based Route to Enhanced Coupling in Nanocrystal Solids. *J. Am. Chem. Soc.* **2011**, *133*, 15753–15761.
24. Nag, A.; Kovalenko, M. V.; Lee, J.-S.; Liu, W.; Spokoyny, B.; Talapin, D. V. Metal-free Inorganic Ligands for Colloidal Nanocrystals: S^{2-}, HS^{-}, Se^{2-}, HSe^{-}, Te^{2-}, HTe^{-}, TeS_3^{2-}, OH^{-}, and NH_2^{-} as Surface Ligands. *J. Am. Chem. Soc.* **2011**, *133*, 10612–10620.
25. Tang, Y.; He, W.; Zhou, G.; Wang, S.; Yang, X.; Tao, Z.; Zhou, J. A New Approach Causing the Patterns Fabricated by Silver Nanoparticles to Be Conductive without Sintering. *Nanotechnology* **2012**, *23*, 355304.
26. Fishelson, N.; Shkrob, I.; Lev, O.; Gun, J.; Modestov, A. D. Studies on Charge Transport in Self-Assembled Gold−Dithiol Films: Conductivity, Photoconductivity, and Photoelectrochemical Measurements. *Langmuir* **2001**, *17*, 403–412.
27. Zabet-Khosousi, A.; Dhirani, A.-A. Charge Transport in Nanoparticle Assemblies. *Chem. Rev.* **2008**, *108*, 4072–4124.
28. Bennett, H. E.; Peck, R. L.; Burge, D. K.; Bennett, J. M. Formation and Growth of Tarnish on Evaporated Silver Films. *J. Appl. Phys.* **1969**, *40*, 3351–3360.
29. Mcmahon, M. D.; Lopez, R.; Meyer, H. M., III; Feldman, L. C.; Haglund, R. F., Jr. Rapid Tarnishing of Silver Nanoparticles in Ambient Laboratory Air. *Appl. Phys. B: Laser Opt.* **2005**, *80*, 915–921.
30. Elechiguerra, J. L.; Larios-Lopez, L.; Liu, C.; Garcia-Gutierrez, D.; Camacho-Bragado, A.; Yacaman, M. J. Corrosion at the Nanoscale: The Case of Silver Nanowires and Nanoparticles. *Chem. Mater.* **2005**, *17*, 6042–6052.
31. Ong, T. H.; Davies, P. B.; Bain, C. D. Adsorption of Thiocyanate on Polycrystalline Silver and Gold Electrodes Studied in Situ by Sum-Frequency Spectroscopy. *J. Phys. Chem.* **1993**, *97*, 12047–12050.
32. Kryukov, A. I.; Stroyuk, A. L.; Zin'chuk, N. N.; Korzhak, A. V.; Kuchmii, S. Y. Optical and Catalytic Properties of Ag_2S Nanoparticles. *J. Mol. Catal. Chem.* **2004**, *221*, 209–221.
33. Chen, R.; Nuhfer, N. T.; Moussa, L.; Morris, H. R.; Whitmore, P. M. Silver Sulfide Nanoparticle Assembly Obtained by Reacting an Assembled Silver Nanoparticle Template with Hydrogen Sulfide Gas. *Nanotechnology* **2008**, *19*, 455604.
34. Dash, U. N.; Mohanty, J.; Panda, K. N. Solubility Studies in Aqueous Media: II. Solubility Product of Silver Thiocyanate and Standard Electrode Potentials of Silver—Silver Thiocyanate Electrode in Aqueous Media. *Thermochim. Acta* **1976**, *16*, 55–61.
35. Talapin, D. V.; Murray, C. B. PbSe Nanocrystal Solids for n- and p-Channel Thin Film Field-Effect Transistors. *Science* **2005**, *310*, 86–89.
36. Oh, S. J.; Berry, N. E.; Choi, J.-H.; Gaulding, E. A.; Paik, T.; Hong, S.-H.; Murray, C. B.; Kagan, C. R. Stoichiometric Control of Lead Chalcogenide Nanocrystal Solids to Enhance Their Electronic and Optoelectronic Device Performance. *ACS Nano* **2013**, *7*, 2413–2421.
37. Liu, Y.; Tolentino, J.; Gibbs, M.; Ihly, R.; Perkins, C. L.; Liu, Y.; Crawford, N.; Hemminger, J. C.; Law, M. PbSe Quantum Dot Field-Effect Transistors with Air-Stable Electron Mobilities above 7 $cm^2\ V^{-1}\ s^{-1}$. *Nano Lett.* **2013**, *13*, 1578–1587.
38. Palik, E. D. *Handbook of Optical Constants of Solids*; Academic Press: San Diego, CA, 1992; Vol. 1.
39. West, P. R.; Ishii, S.; Naik, G. V.; Emani, N. K.; Shalaev, V. M.; Boltasseva, A. Searching for Better Plasmonic Materials. *Laser Photonics Rev.* **2010**, *4*, 795–808.
40. Naik, G. V.; Boltasseva, A. A Comparative Study of Semiconductor-Based Plasmonic Metamaterials. *Metamaterials* **2011**, *5*, 1–7.
41. Ho, C.-M.; Yau, S. K.-W.; Lok, C.-N.; So, M.-H.; Che, C.-M. Oxidative Dissolution of Silver Nanoparticles by Biologically Relevant Oxidants: A Kinetic and Mechanistic Study. *Chem.−Asian J.* **2010**, *5*, 285–293.
42. Levard, C.; Hotze, E. M.; Lowry, G. V.; Brown, G. E. Environmental Transformations of Silver Nanoparticles: Impact on Stability and Toxicity. *Environ. Sci. Technol.* **2012**, *46*, 6900–6914.
43. Vignos, J. C. Means of Cleaning and Protecting Metal Surfaces. US1750651 A, March 18, 1930.
44. Damrath, J. J. G. Lubricants Containing an Amino Thiocyanate and a Cyclic Amine. US3330763 A, July 11, 1967.
45. Yu, W. W.; Falkner, J. C.; Shih, B. S.; Colvin, V. L. Preparation and Characterization of Monodisperse PbSe Semiconductor Nanocrystals in a Noncoordinating Solvent. *Chem. Mater.* **2004**, *16*, 3318–3322.